

This article appeared in ***Opt. Express* 33, 41473-41488 (2025)** and may be found at URL: <https://opg.optica.org/oe/fulltext.cfm?uri=oe-33-20-41473###>.

Open Access This article is licensed under a Creative Commons Attribution-NonCommercial-NoDerivatives 4.0 International License, which permits any non-commercial use, sharing, distribution and reproduction in any medium or format, as long as you give appropriate credit to the original author(s) and the source, provide a link to the Creative Commons licence, and indicate if you modified the licensed material. You do not have permission under this licence to share adapted material derived from this article or parts of it. The images or other third party material in this article are included in the article's Creative Commons licence, unless indicated otherwise in a credit line to the material. If material is not included in the article's Creative Commons licence and your intended use is not permitted by statutory regulation or exceeds the permitted use, you will need to obtain permission directly from the copyright holder. To view a copy of this licence, visit <http://creativecommons.org/licenses/bync-nd/4.0/>. © The Author(s) 2025

<https://doi.org/10.1038/s41528-025-00457-w>

Robust and flexible organic electrochemical transistors enabled by electropolymerized PEDOT

Check for updates

Meijing Wang¹, Jiaxin Fan¹, Michel Bilodeau-Calame¹, Chihyeong Kim¹, Cheng-Ling Chiang¹,
Ademar Fabricio Chaverri Segura¹, Vito Vurro^{2,3}, Ilaria Bargigia^{2,4}, Janine Mauzeroll⁵ & Fabio Cicoira¹ ✉

Organic electrochemical transistors (OECTs) based on poly(3,4-ethylenedioxythiophene) (PEDOT) have been extensively studied, yet devices fabricated via electropolymerization remain underexplored in terms of the underlying ionic dynamics and the potential for flexible integration. In this work, we demonstrate robust OECTs based on electropolymerized PEDOT, exhibiting negligible drain current degradation after 1000 cycles of operation in aqueous NaCl. Compared to inkjet-printed devices, they offer markedly superior cycling stability, which is further enhanced by the incorporation of the small anionic dopant ClO_4^- . We also show flexible, lightweight OECTs by electropolymerizing PEDOT on ultrathin parylene substrates, achieving stable performance under mechanical strain. Furthermore, Electrochemical Quartz Crystal Microbalance with Dissipation (EQCM-D) analysis reveals distinct ion transport behavior in PEDOT: ClO_4^- , where dopant ejection dominates doping/dedoping process, unlike in PEDOT:PSS. This study underscores the advantages of electropolymerization and small-ion doping, offering new mechanistic insights and advancing the design of high-performance, flexible OECTs for bioelectronic applications.

Organic electrochemical transistors (OECTs), characterized by their mixed ionic-electronic conducting properties, low operation voltages, and high amplification capability, have garnered significant attention in recent years¹. These attractive features make OECTs promising candidates for a broad range of bioelectronic applications^{2,3}, including biosensors⁴, artificial synapses⁵, and neuromorphic computing⁶. OECTs are three-terminal devices, which consist of an active material film that connects the source and drain electrodes, forming the channel of the device. This channel material is in direct contact with a gating medium⁷, typically a liquid or gel electrolyte, which in turn is in contact with the gate electrode. Organic mixed ionic-electronic conductors (OMIECs), which exhibit both ionic and electronic conduction, are used as channel materials⁸. During OECTs operation, reversible electrochemical doping/dedoping of the channel occurs when a gate voltage is applied, leading to current modulation^{1,9}. The most extensively studied OECTs are based on poly(3,4-ethylenedioxythiophene) (PEDOT), usually doped with the polyanion, poly(styrenesulfonate) (PSS)^{10–13}, owing to its high conductivity, biocompatibility, chemical and electrochemical stability, and versatile processibility¹⁴ via spin-coating¹⁵, drop-casting¹⁶, screen printing¹⁷, direct-ink writing^{18,19}, inkjet printing²⁰, and aerosol jet printing²¹. Most of these techniques rely on commercial PEDOT:PSS suspensions. Electropolymerized PEDOT-based OECTs, along with their performance and working mechanisms, have received comparatively less attention.

Interestingly, electropolymerization was the first technique used to fabricate OECTs in the mid 1980s^{22–25}. In recent years, this approach has regained interest for producing OECTs aimed at advanced applications, including biomimetic neuromorphic sensing^{26,27}, dendritic networks for brain-inspired computation^{28,29}, and biofunctionalized biosensors^{30–33}. For OECTs with vertical geometry, electropolymerization enable precise channel deposition, resulting in exceptional device performance³⁴. Electropolymerization offers several advantages for processing OECTs, enabling precise control over the channel's chemical composition through the incorporation of various doping counterions, as well as tunable thickness and morphology by adjusting processing parameters. Aside from simplicity of equipment and short deposition time, the minimal use of solvents, monomers and dopants during processing makes this technique environmentally friendly. This method holds great potential for developing bioelectric interfaces, such as PEDOT-coated neural probes for stimulation^{35,36}. However, electropolymerization requires conductive substrates, which poses challenges for achieving uniform film coverage across the insulating channel regions of transistors. This limitation has also hindered the development of electrodeposition for fabricating flexible OECTs. Research on electrodeposited OECTs is still in its early stage. Studies of OECTs based on PEDOT doped with three different counterions, i.e., PSS⁻, p-toluene sulfonate (pTS⁻), and perchlorate (ClO_4^-), revealed that the highest drain currents and maximum transconductances were achieved with the

¹Department of Chemical Engineering, Polytechnique Montréal, Montréal, QC, Canada. ²Center for Nanoscience and Technology, Italian Institute of Technology, Milan, Italy. ³Department of Physics and Astronomy, University of Bologna, Bologna, Italy. ⁴Physics Department, Politecnico di Milano, Milan, Italy. ⁵Department of Chemistry, McGill University, Montréal, QC, Canada. ✉e-mail: fabio.cicoira@polymtl.ca

medium-sized counterion, pTS^{-37} . Relevant studies on OECTs fabricated through electropolymerization are summarized in Supplementary Table 1.

The working principle of OECTs relies on ionic-electronic coupling effects, where ions moving in and out from the channel material led to current modulation. Electrochemical Quartz Crystal Microbalance (EQCM) is a powerful operando technique for monitoring mass variation of OMIEC films during bias application, enabling quantification of ionic injection and ejection throughout the doping and dedoping processes that drive OECT operation^{38,39}. EQCM has been employed to investigate the mechanism of OECTs fabricated by spin-coating commercial PEDOT:PSS crosslinked with (3-glycidyloxypropyl)trimethoxysilane (GOPS), where the PSS^{-} dopant counterions remain immobile. Studies conducted in aqueous NaCl demonstrated that dedoping is predominately driven by the injection of Na^{+} cations into the channel material, resulting in decreased channel conductance⁴⁰. A combined EQCM and ex situ X-ray fluorescence (XRF) study on PEDOT:PSS films treated with sulfuric acids revealed that both anions and cations participate in the doping and dedoping processes⁴¹. Differences in the doping/dedoping mechanisms between acid-treated and ethylene glycol-treated crosslinked PEDOT:PSS, where only cations participate in the doping and dedoping processes, were confirmed through XRF quantitative analysis⁴². For OECTs based on electropolymerized conducting polymers doped with various ions (e.g., PEDOT:PSS and PEDOT: ClO_4), EQCM studies would be particularly valuable in elucidating the working mechanism. While large immobile counterions, such as PSS^{-} , remain in the film during the doping-dedoping process, smaller mobile counterions may be ejected during dedoping, leading to a more complex operational mechanism. The working mechanism can be extended to flexible and stretchable transistors, advancing the understanding of underlying processes for flexible electronics.

In this work, we investigated OECTs based on electropolymerized PEDOT: ClO_4 and PEDOT:PSS, representing two model systems with immobile and mobile dopants, respectively. By comparing device performance in aqueous NaCl, we observed that the smaller ClO_4^{-} dopant facilitates a fully doped state for PEDOT. Additionally, electropolymerization enhanced the cycling stability of OECTs, compared to devices based on printed commercial suspensions. We also fabricated lightweight and flexible OECTs based on the electropolymerized PEDOT: ClO_4 film on a thin parlylene substrate. To clarify the working mechanism of electropolymerized OECTs, we employed EQCM to study the doping and dedoping processes. For PEDOT:PSS, the process is predominantly governed by the injection and ejection of Na^{+} ions from the electrolyte. In contrast, for PEDOT: ClO_4 , dedoping also involves the ejection of the ClO_4^{-} dopant counterions.

Results

High-performance OECTs based on electropolymerized small-anion doped PEDOT

The main challenge in fabricating electropolymerized OECTs is depositing the channel material onto insulating substrates. This can be addressed by short-circuiting metal source-drain electrodes, spaced by a moderately small gap (typically less than 50 μm), and using them as a single working electrode during electropolymerization⁴³. This setup enables the formation of a continuous channel by bridging the insulating gap between the electrodes with the electropolymerized material. Other approaches include using alternating current to promote fiber formation along the direction of the electric field, eventually creating dendritic networks^{44,45}, and pre-coating the channel area with solution-processed PEDOT^{46,47}.

We electropolymerized PEDOT: ClO_4 films onto short-circuited source-drain electrodes patterns to fabricate OECTs (Fig. 1a) using

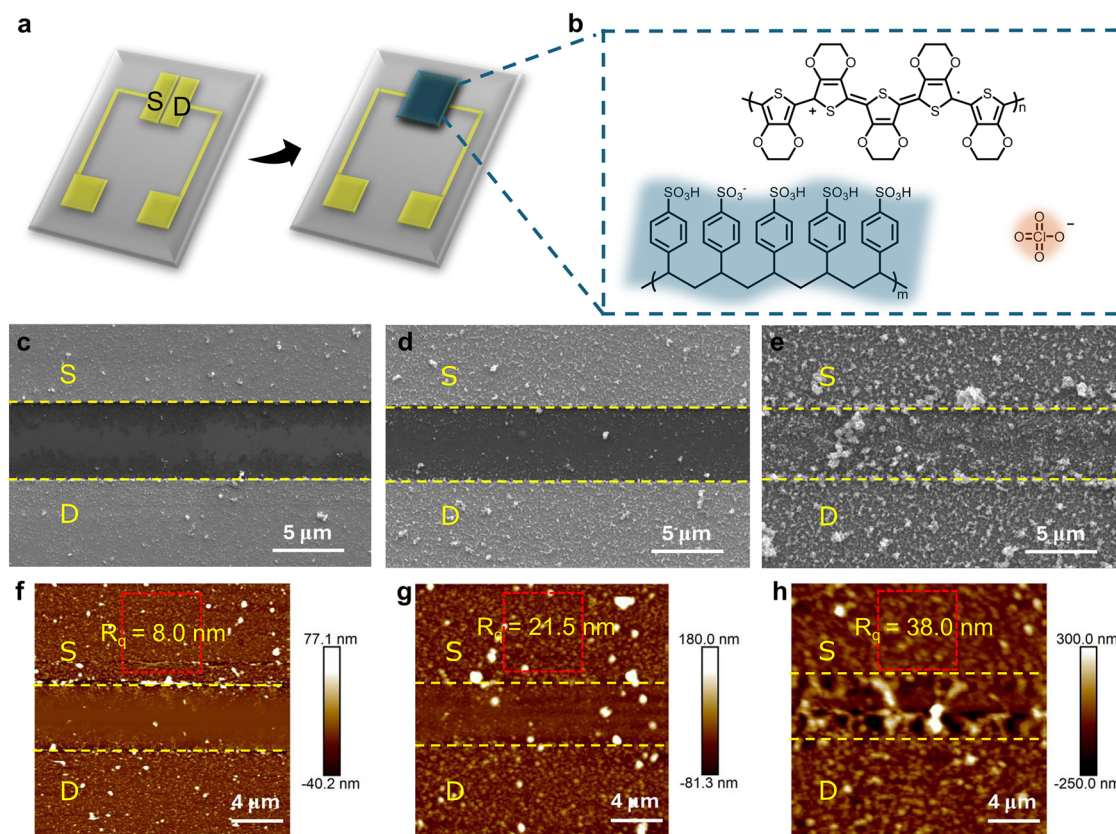


Fig. 1 | Morphology characterizations of electrodeposited films. **a** Schematic illustration of the OECT structure with patterned Au source (S)-drain (D) electrodes and electrodeposited PEDOT channel film. **b** Chemical structure of PEDOT⁺, PSS⁻ and ClO_4^{-} . SEM (c–e) and AFM (f–h) images of PEDOT: ClO_4 films

electropolymerized at charge densities of: **c, f** 20 mC/cm^2 , **d, g** 30 mC/cm^2 and **e, h** 60 mC/cm^2 . Yellow dashed lines: OECT channel. Red dashed box: region from which the surface roughness R_q is extracted.

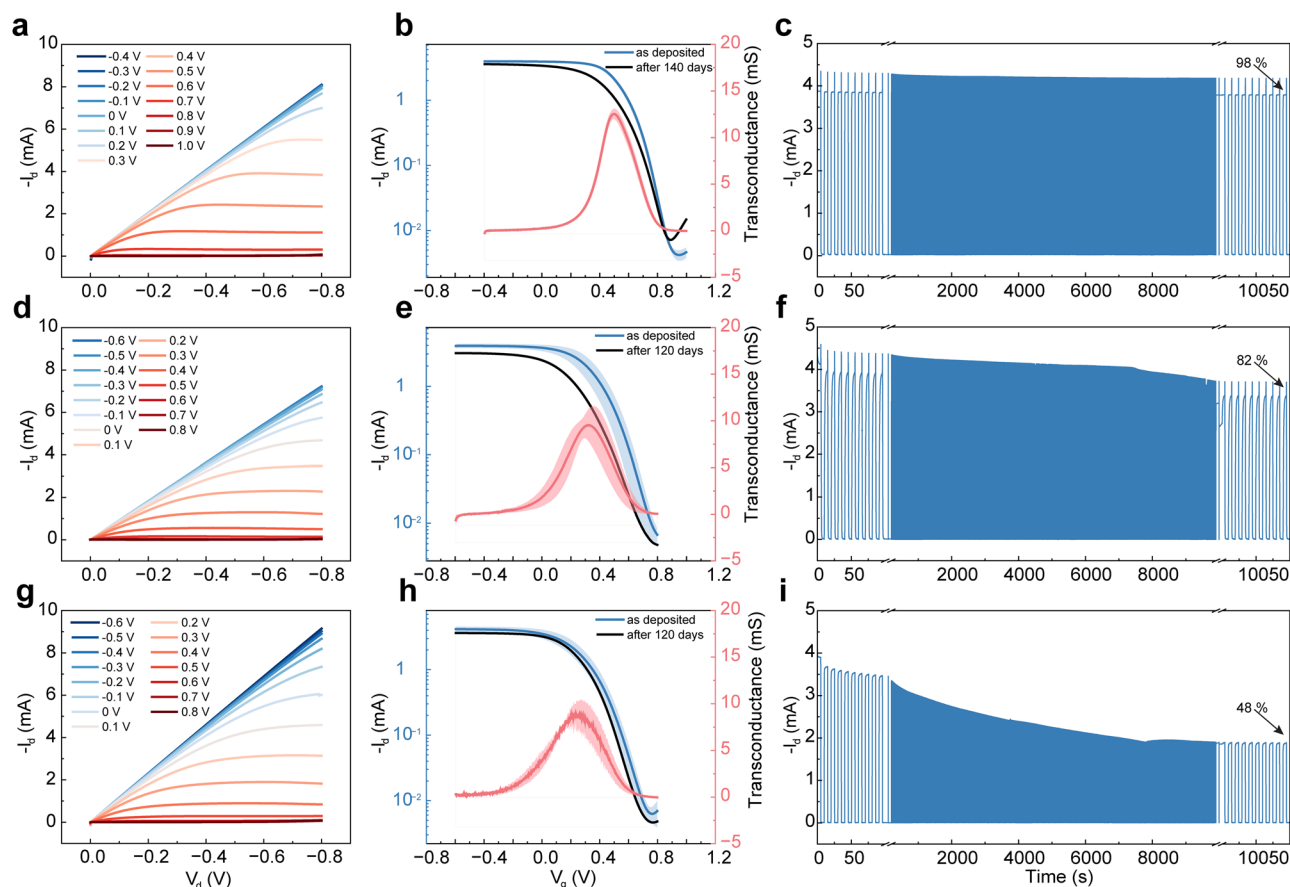


Fig. 2 | Output (I_D - V_D), transfer (I_D - V_G) characteristics (measured as deposited and after long time storage), transconductance (g_m), and cycling stability within 1000 cycles for OECTs. a–c electropolymerized PEDOT: ClO_4 with deposition charge density of 60 mC/cm^2 ; **d–f** electropolymerized PEDOT:PSS with deposition charge density of 300 mC/cm^2 ; **g–i** ink-jet printed PEDOT:PSS. A Ag/AgCl pellet

gate and 100 mM NaCl electrolyte were used in all measurements. Transfer curves were measured at a $V_D = -0.4 \text{ V}$. For all fabrication conditions, three devices were measured to confirm their reproducibility. All samples were measured one day after fabrication. The shaded area around the transfer curves represents the standard deviation extracted from three samples. $W/L = 4000 \text{ }\mu\text{m}/5 \text{ }\mu\text{m}$.

varying concentrations (1, 5, 100 mM) of the dopant LiClO_4 . All devices exhibited p-type behavior and operated in depletion mode, as expected for PEDOT-based OECTs¹⁸. Notably, electrolyte concentrations of 5 mM and 100 mM both resulted in complete channel coverage, yielding OECTs with similar electrical characteristics (Supplementary Fig. 1). In contrast, a 1 mM concentration was insufficient to bridge source and drain electrodes, as no significant current was detected during electrical measurements. We consistently used high concentration of 100 mM in this study, as it is commonly employed in electrochemical systems for its high ionic conductivity and reduced ionic migration⁴⁸.

The morphology of PEDOT: ClO_4 films electrodeposited at charge densities of 20 (Fig. 1c, f), 30 (Fig. 1d, g), and 60 (Fig. 1e, h) mC/cm^2 was investigated using scanning electron microscopy (SEM) and atomic force microscopy (AFM). As expected, electropolymerization initiated at the Au electrodes and progressively extended across the channel area, with growth occurring both laterally and vertically relative to the electrode surface. This behavior aligns with established nucleation-growth mechanisms, resulting in a progressive increase in surface roughness (root mean square roughness, R_q) at longer deposition times⁴⁹. At an early stage (20 mC/cm^2 , 40 s), the film primarily formed on the source and drain electrodes, with limited extension into the adjacent channel regions. The resulting morphology displayed an R_q of 8 nm (Fig. 1c, f). Increasing the deposition charge (30 mC/cm^2 , 60 s) led to full channel coverage, yielding a granular network on the Au electrodes ($R_q = 21 \text{ nm}$, Fig. 1d, g; Supplementary Fig. 2a) and densely packed aggregates across the channel (Supplementary Fig. 2b). Further increasing the deposition charge (60 mC/cm^2 , 120 s) led to continued film growth atop the existing PEDOT layer, producing a rougher granular morphology across

both the electrodes and channel ($R_q = 38 \text{ nm}$, Fig. 1e, h; Supplementary Fig. 2c). Although the morphological image does not show a complete connection between the source and drain electrodes at low deposition charge (20 mC/cm^2 , Fig. 1c, f), localized conductive pathways may lead to devices showing a low source-drain current and a limited performance in terms of transconductance (0.1 mS) and ON/OFF ratio (2×10^1) (Supplementary Fig. 3a, d). When the channel was fully covered, at 30 mC/cm^2 (Supplementary Fig. 3b, e) and 60 mC/cm^2 (Supplementary Fig. 3c, f), the devices displayed similar performance with high transconductance (above 10 mS), and an ON/OFF ratio around 1×10^3 , despite minor changes in morphology (Supplementary Fig. 2). Electrodeposited OECTs obtained with other small dopants (Supplementary Fig. 4), such as LiBF_4 and TEABF_4 , frequently used for PEDOT electrodeposition, showed similar transconductance ($\sim 10 \text{ mS}$) and ON/OFF ratios ($\sim 4 \times 10^2$), indicating that various combinations of small anion dopants and accompanying cations do not significantly impact the electropolymerization process, consistent with previous findings⁵⁰. Overall, our results show that electrodeposition produces highly reproducible devices with performance comparable to state-of-the-art electropolymerized OECTs (Supplementary Table 1).

Devices with similar steady-state characteristics (Fig. 2) were obtained using the larger polymeric dopant polystyrene sulfonate (PSS), both through electrodeposition ($g_m \sim 10 \text{ mS}$, ON/OFF ratio $\sim 6 \times 10^2$) and inkjet printing from a commercial suspension ($g_m \sim 9 \text{ mS}$, ON/OFF ratio $\sim 7.4 \times 10^2$) (Table 1). Notably, the drain current (I_D) saturated at $\sim V_G = 0 \text{ V}$ for PEDOT: ClO_4 OECTs (Fig. 2a, b, and Supplementary Fig. 5a, d), but at a slightly negative V_G for the electropolymerized (Fig. 2d, e, and Supplementary Fig. 5b, e) and printed (Fig. 2g, f, and Supplementary Fig. 5c, f)

Table 1 | Figures of merit of the OECTs reported in this work

Channel material	Fabrication method	Dopant concentration (mM)	Deposition charge density (mC/cm ²)	Transconductance (mS)	ON/OFF ratio ($\times 10^3$)
PEDOT:ClO ₄	electropolymerization	100 mM	30	11.0 \pm 1.0	1.0 \pm 0.1
PEDOT:ClO ₄	electropolymerization	100 mM	60	13.0 \pm 0.5	1.0 \pm 0.2
PEDOT:BF ₄ (TEABF ₄)	electropolymerization	100 mM	60	9.0	0.3
PEDOT:BF ₄ (TEABF ₄)	electropolymerization	5 mM	60	11.0	0.3
PEDOT:BF ₄ (LiBF ₄)	electropolymerization	100 mM	60	10.0	0.5
PEDOT:BF ₄ (LiBF ₄)	electropolymerization	5 mM	60	8.0	0.4
PEDOT:PSS	electropolymerization	100 mM	300	10.0 \pm 1.4	0.6 \pm 0.1
PEDOT:PSS	ink-jet printing	N/A	N/A	9.0 \pm 1.0	0.7 \pm 0.2
PEDOT:ClO ₄ (on parylene)	electropolymerization	100 mM	60	7.5	0.25

PEDOT:PSS OECTs. This indicates that, at $V_G = 0$ V, PEDOT:ClO₄ films are fully doped, while PEDOT:PSS films are partially doped. This is further supported by UV-Vis spectroscopic measurements, which are discussed in detail in the following section. Therefore, PEDOT:ClO₄ devices can operate with lower energy consumption. These findings demonstrate that the ClO₄⁻ dopant promotes a fully doping state in PEDOT films, likely due to the more efficient insertion and redistribution of the smaller dopant ions during electrodeposition. Remarkably, all devices retained similar performance after 4 months of storage in ambient conditions (Fig. 2b, e, h).

Despite their similar steady-state performance, the devices exhibited different stability under cyclic pulsed V_G application. To assess cycling stability, we monitored current responses during gate voltage pulses ($V_G = 0.8$ V, pulse width = 5 s) over time. For PEDOT:ClO₄ OECTs, the current (I_D) remained nearly constant, with only a 2% decrease after 1000 cycles (Fig. 2c). Electrodeposited PEDOT:PSS-OECTs showed a roughly 20% decline in I_D (Fig. 2f). A larger I_D drop of about 50% was observed in printed devices (Fig. 2i). The reduced cycling stability of PEDOT:PSS is primarily attributed to the greater swelling of its hydrophilic PSS chains^{51–53}. In inkjet-printed devices, this effect is more pronounced due to the excess PSS required to stabilize commercial PEDOT:PSS dispersions. The higher PSS content increases film hydrophilicity, leading to enhanced swelling in aqueous environments and reduced operational stability. This observation is consistent with our previous findings: solution-processed PEDOT:PSS films showed a significant weight increase after 10 min of water immersion, whereas PEDOT:ClO₄ films exhibited minimal change⁵⁴. Beyond swelling, differences in channel/electrode interface quality, arising from distinct fabrication methods, may also contribute to the observed performance variations. Overall, electropolymerized OECTs demonstrated superior stability compared to printed devices, particularly when the small dopant anion ClO₄⁻ was used. While inkjet printing is widely used for fabricating flexible electronic devices, the advantages of electropolymerization underscore its promising potential for the development of flexible OECTs.

Electropolymerized PEDOT:ClO₄ on parylene substrate for flexible and lightweight OECTs

Flexible and lightweight OECTs were fabricated by electropolymerizing PEDOT:ClO₄ films onto source-drain electrodes patterned on a thin (10 μ m) parylene layer deposited on a glass substrate. At the end of the fabrication process, the parylene layer was peeled off from the glass to yield ultrathin flexible devices (Fig. 3a). Compared to conventional flexible substrates such as polyimide or polyethylene terephthalate (PET), ultrathin parylene films significantly reduce overall device weight and allow conformability to small-radius curved surfaces, facilitating mechanical flexibility testing. The ability of a material to conform to curved surfaces is governed by its bending stiffness, which is proportional to the Young's modulus (E) and the cube of its thickness (t^3). For a given material, where the Young's modulus is constant, reducing the thickness significantly lowers the bending stiffness, allowing it to bend more easily and conform to surfaces

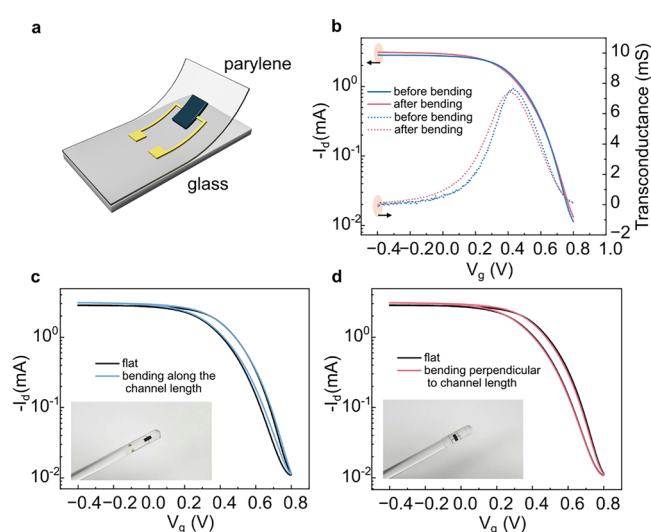


Fig. 3 | Fabrication and electrical characteristics of flexible OECTs based on electropolymerized PEDOT:ClO₄ on a parylene substrate. **a** Schematic illustration of the flexible OECT. Transfer characteristics of the flexible OECT measured **b** before mechanical bending and after recovery from mechanical bending; **c** at the flat state and under bending parallel to the channel length; **d** at the flat state and under bending perpendicular to the channel length. (Insets: photographs of the device bending along different directions on a glass rod with the diameter of 5 mm).

with smaller radii of curvature. In the flat state, the flexible devices exhibited a transconductance of 7.6 mS and an ON/OFF ratio of 2.5×10^2 (Fig. 3b), slightly lower than those of the rigid counterparts, likely due to variations in PEDOT film growth influenced by differences in gold electrode surfaces across substrates (Supplementary Fig. 6). Importantly, the transfer characteristics remained nearly unchanged under mechanical deformation applied either parallel (Fig. 3c) or perpendicular (Fig. 3d) to the channel length, demonstrating robust flexibility in both directions. After recovery from bending, the devices retained a transconductance of 7.4 mS and an ON/OFF ratio of 2.3×10^2 , confirming stable performance after mechanical strains. Further evaluation of mechanical durability and long-term reliability in future will be important for advancing their practical application in flexible electronics.

Electrochromic behavior of PEDOT:ClO₄ films during doping/dedoping monitored by UV-Vis spectroelectrochemistry

UV-Vis spectroelectrochemistry has been widely used to study changes in doping state of conducting polymers during electrochemical doping and dedoping processes⁵⁵. For our study, we monitored the UV-Vis absorption spectra of electrodeposited PEDOT:ClO₄ films in real time while applying cyclic linear voltage sweeps between -1.0 and 0.4 V, effectively capturing

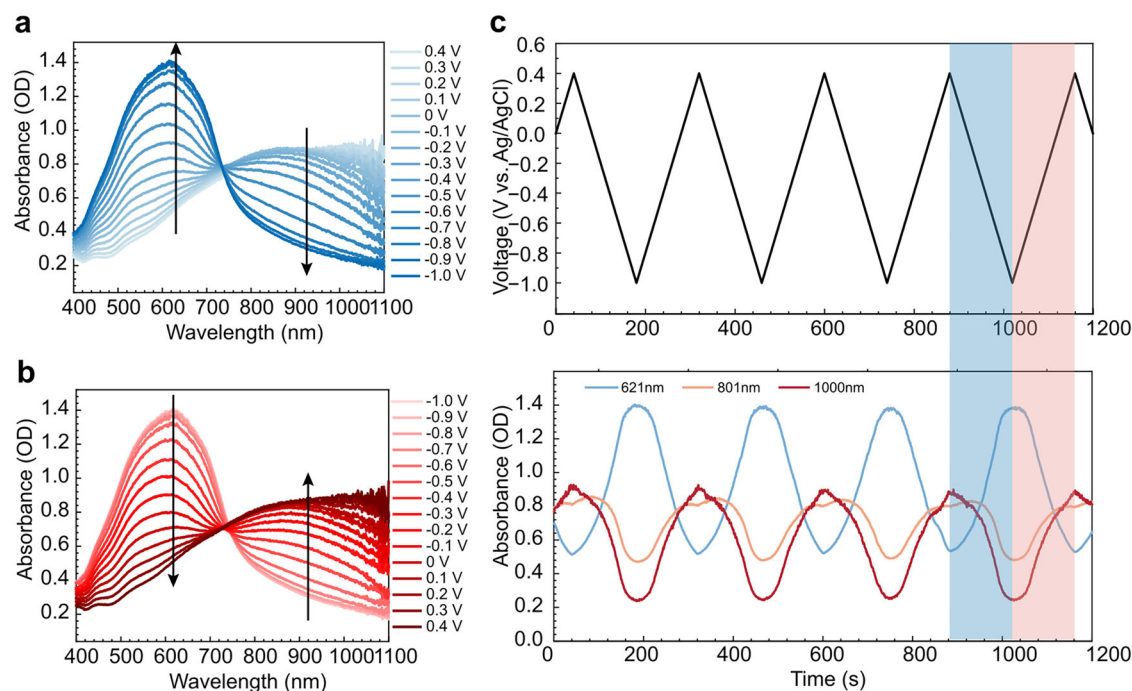


Fig. 4 | Spectroelectrochemical measurements of PEDOT:ClO₄ films electro-deposited from a 100 mM dopant solution. Real-time absorption spectra during a dedoping (+0.4 to −1.0 V) and b redoping (−1.0 to +0.4 V) presented with 0.1 V

increments. c top layer: voltage sweep, lower layer: temporal behavior of the three wavelengths chosen as representative of neutral chains (621 nm), polarons (801 nm), and polarons + bipolarons (1000 nm).

the dedoping (Fig. 4a) and redoping (Fig. 4b) processes. Consistent with prior studies on PEDOT films⁵⁶, we observed a characteristic absorbance band in the 400–700 nm range, which corresponds to the π – π^* transitions of PEDOT neutral chains. Additionally, a second band appeared in the near-infrared range (700–1100 nm), associated with polaron absorption. The bipolaron states, which are typically located in the far infrared range, were not captured in our spectra. To analyze these changes more closely, we monitored selected wavelengths over time (Fig. 4c lower panel): the 621 nm curve (blue line), representing neutral chain signatures, increased significantly as the potential shifted from 0.4 to −1.0 V (Fig. 4c top panel). Simultaneously, the 801 nm (pale red line) and the 1000 nm (red line) curves, corresponding to the polaron band, decreased, consistent with the dedoping of the polymer film. During the redoping process, within the polaron absorption region (800 nm and 1000 nm), a unique behavior was observed near the highly doped state (around 0.4 V). The 800 nm peak displayed a dip, while the 1000 nm peak reached maximum intensity. In contrast, the 621 nm signal continued to decrease. These features suggest that, while the number of neutral chains decreases during redoping, the polarons do not increase to their maximum concentration but instead transition into other species, possibly bipolarons. This observation aligns with the idea that, under highly doped conditions, some polarons convert to bipolarons, indicating complex dynamics in the electronic states of PEDOT under different electrochemical conditions.

Similar results were observed for films electrodeposited from a 5 mM solution (Supplementary Fig. 7), indicating that dopant concentration has minimal impact on the electrical modulation of electropolymerized PEDOT films. This finding aligns with the comparable performance observed in OECTs, reinforcing that variations in dopant concentration do not significantly influence the electronic properties and functionality of these films.

UV–Vis spectroscopic comparison of PEDOT:ClO₄ and PEDOT:PSS at 0 V bias highlights distinct differences in their doping states (Supplementary Fig. 8). PEDOT:PSS displays a pronounced absorption band between 600 and 800 nm (black shaded area), while PEDOT:ClO₄ exhibits stronger absorption beyond 900 nm (red shaded area). The latter is indicative of increased bipolaron formation, as previously discussed, and reflects a higher doping level in the electropolymerized PEDOT:ClO₄ film.

Different ionic injection/ejection behaviors for PEDOT:ClO₄ and PEDOT:PSS measured by EQCM-D

To further investigate the doping and dedoping mechanisms in the devices, we employed Electrochemical Quartz Crystal Microbalance with Dissipation (EQCM-D) to monitor in situ mass changes of the channel materials under applied bias in aqueous NaCl. The changes in resonance frequency ($\Delta f/n$) and dissipation (ΔD) across multiple harmonics were recorded during cyclic linear potential sweeps, allowing us to gain insight into the dynamic mass uptake and release associated with electrochemical modulation. This approach provides valuable information on how mass transport correlates with the electronic state changes within the channel materials during the doping and dedoping processes, for both rigid and flexible devices.

For quantitative mass analyses, the mass variation (Δm) at the sensor surface or within the deposited film can be determined from the recorded oscillation frequency change (Δf) across different overtones orders (n) using the Sauerbrey's equation (Eq. 1):

$$\Delta m = -\frac{Z_q}{2f_0^2} \times \frac{\Delta f}{n} = -C \times \frac{\Delta f}{n} \quad (1)$$

where $\Delta f/n$ is the change of frequency at n th overtone. $C = Z_q/2f_0^2$ is the calculation constant (or sensitivity factor) of the quartz crystal, where f_0 is the fundamental resonance frequency, and Z_q is the acoustic impedance of the quartz crystal ($\sim 8.8 \times 10^5$ g/cm²s). For a 5 MHz crystal sensor, C equals 17.7 ng/cm²Hz⁵⁷.

According to the Sauerbrey equation, an increase in $\Delta f/n$ corresponds to a mass loss, and a decrease corresponds to a mass gain. This equation is typically applicable to rigid materials, such as metal coatings, in air or liquid⁵⁸. For polymer coatings in contact with liquid media, the Sauerbrey model remains valid if the dissipation change is minimal ($\Delta D \approx 0$); otherwise, viscoelastic models are preferable⁵⁸. It has been shown that for polymer films thinner than 100 nm, the Sauerbrey model reliably reflects mass changes (Δm)^{40,41}. When dissipation changes are small, the frequency shifts ($\Delta f/n$) overlap across all measured harmonics, indicating that the film behaves as a rigid layer firmly attached to the sensor surface⁵⁹. In our

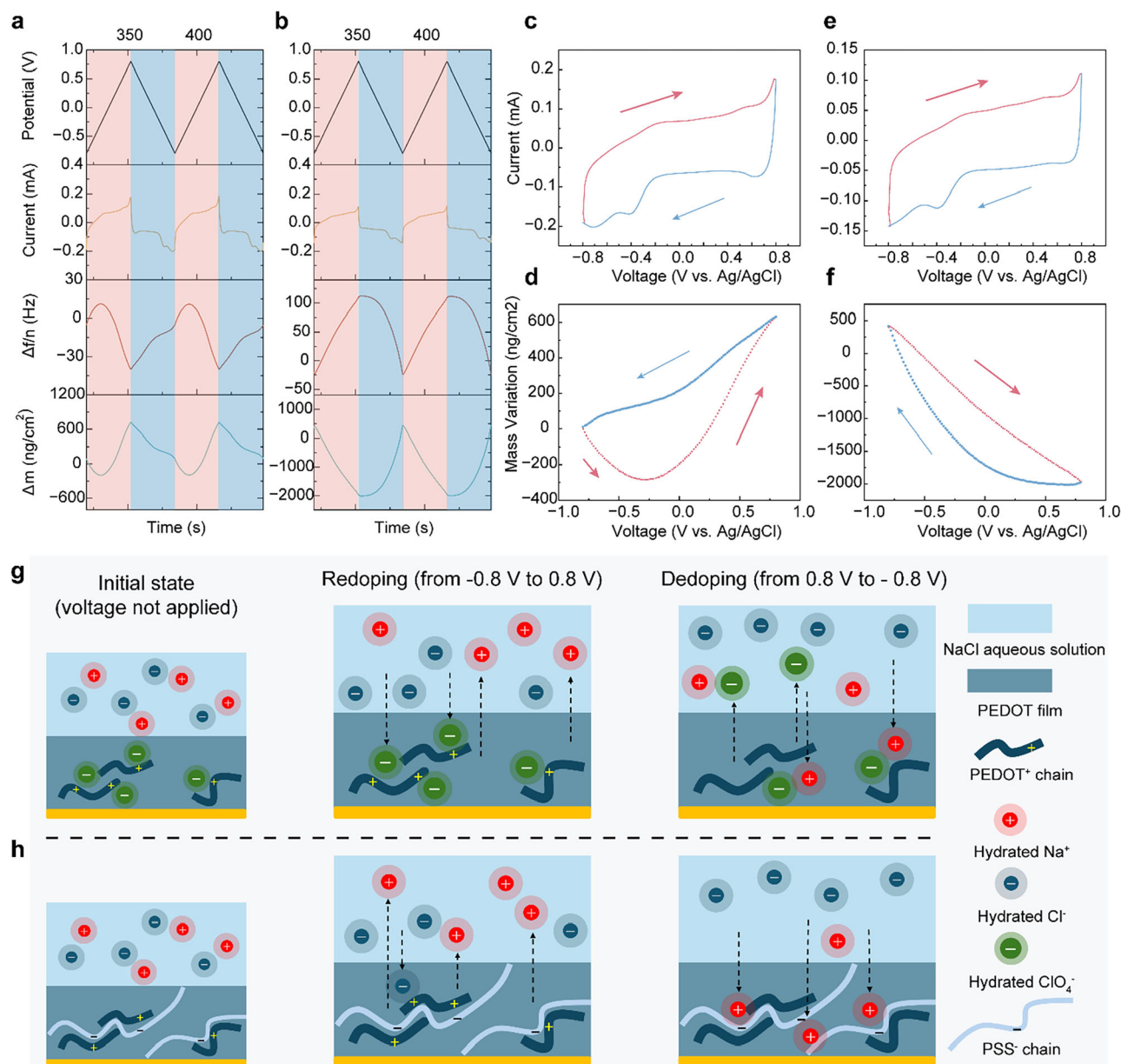


Fig. 5 | EQCM-D behavior of PEDOT:ClO₄ and PEDOT:PSS films electro-deposited over 30 s on EQCM quartz crystals. Voltage sweep, current response, frequency response ($\Delta f/n$) at the 3rd overtone, and converted mass variation (Δm) under cyclic linear potential sweep for a PEDOT:ClO₄ and **b** PEDOT:PSS. The potential was applied between -0.8 V to 0.8 V at a scan rate of 50 mV/s. **c** Cyclic voltammetry, **d** mass variation vs. voltage for PEDOT:ClO₄. **e** Cyclic voltammetry,

f mass variation vs. voltage for PEDOT:PSS. Illustration of the ionic distribution without voltage application and during redoping/dedoping **g** for PEDOT:ClO₄ and **h** for PEDOT:PSS. The bottom yellow part indicates the Au QCM sensor. For (**a** and **b**), the data from the 5th and 6th cycles are shown, and for (**c-f**), the 5th cycle is plotted.

experiments, all electrodeposited films showed negligible shifts of $\Delta f/n$ and ΔD over a complete cycle, spanning voltage sweeps from -0.8 to $+0.8$ V and back (Supplementary Figs. 9, 10). This behavior suggests minimal ionic accumulation or loss, indicating stable mass dynamics during the electrochemical modulation processes.

The EQCM-D responses for PEDOT:ClO₄ and PEDOT:PSS films deposited over a 30-s period showed negligible changes in ΔD , along with overlapping $\Delta f/n$ values across different overtones ($n = 3, 5,$ and 7) (Supplementary Fig. 9a, b), indicating that these films could be reliably analyzed for mass transport. The cyclic voltammograms (CV) for PEDOT:ClO₄ (Fig. 5c and Supplementary Fig. 11c) exhibited the typical shape of CV for PEDOT⁶⁰, with increasing current at faster scan rates, suggesting a pseudo-capacitive behavior. A similar CV profile was observed for PEDOT:PSS (Fig. 5e). The peak observed at -0.4 V, which diminishes upon degassing

(Supplementary Fig. 12), is related to oxygen electrochemistry under normal operating conditions.

Before a full cycle sweep, the PEDOT films were held at -0.8 V to achieve a fully dedoped state, due to the injection of the Na⁺ ions from the electrolyte and, where feasible, the ejection of mobile dopant anions. During the subsequent voltage sweep from -0.8 to 0.8 V (redoping), electrolyte cations migrate toward the counter electrode, while anions migrate to the PEDOT working electrode and enter the film. The ionic movement occurs oppositely during the reverse sweep from 0.8 to -0.8 V (dedoping).

The mass changes for PEDOT:ClO₄ during CV were determined from the frequency responses at the 3rd overtone across different voltage scan rates: 20 mV/s (Supplementary Fig. 11a), 50 mV/s (Fig. 5a), and 100 mV/s (Supplementary Fig. 11b). Illustrations of the ionic distribution at the initial state (without voltage applied), during redoping (from -0.8 V to 0.8 V) and

during dedoping (from 0.8V to -0.8 V) are provided for PEDOT:ClO₄ (Fig. 5g) and PEDOT:PSS (Fig. 5e). These mass variations correlated closely with the voltage and current profiles at all scan rates, with only minor differences observed (Supplementary Fig. 11d), indicating that ionic movement is minimally impacted by scan rate. For PEDOT:ClO₄, redoping (Fig. 5a, pink shaded area, and Fig. 5d, pink line) begins with a decrease in Δm between -0.8 to -0.3 V due to the ejection of Na⁺ ions (Fig. 5g). Beyond -0.3 V, Δm sharply increases as ClO₄⁻ dopant anions (Fig. 5g), previously ejected during dedoping, re-enter the film possibly accompanied by Cl⁻ anions from the electrolyte. During the reverse sweep (dedoping), Δm continuously decreases (Fig. 5a blue shaded area, and Fig. 5d, blue line), indicating that ClO₄⁻ and Cl⁻ anions leave the film as Na⁺ ions are injected (Fig. 5g). PEDOT:ClO₄ samples deposited for 60 s and 120 s exhibited larger ΔD values and pronounced $\Delta f/n$ splitting across different overtones $n = 3, 5$ and 7 (Supplementary Fig. 10), suggesting that the Sauerbrey equation is no longer applicable. It has been reported that higher-order shear waves are more sensitive to the material near the electrodes, while lower-order waves experience less damping in the film. Frequency shifts were smaller at higher-order overtones and larger at lower-order overtones, indicating that mass changes are more pronounced closer to the electrolyte. This observation differs from the case of acid-treated PEDOT:PSS, which has been reported to exhibit greater mass change near the substrate³⁹.

For PEDOT:PSS, during redoping, a substantial mass decrease was observed (Fig. 5b pink shaded area, Fig. 5f pink line), indicating that the process is primarily driven by the ejection of Na⁺ cations from the film, along with the injection of Cl⁻ anions (Fig. 5h). During dedoping, Δm remained stable from 0.8 to 0.4 V but increased between 0.4 and -0.8 V (Fig. 5b blue shaded area, Fig. 5f blue line). The stable Δm between 0.8 and 0.4 V suggests a mass balance between the slight ejection of Cl⁻ ions and the injection of Na⁺ ions. The subsequent mass increase indicates that the process is dominated by Na⁺ ion injection to compensate negatively charged PSS chain (Fig. 5h), consistent with the widely accepted understanding of the doping/dedoping mechanism in PEDOT:PSS. Unlike previous findings regarding spin-coated PEDOT:PSS films containing additives⁴⁰, our results demonstrate the participation of Cl⁻ anions in this process.

Therefore, EQCM-D enabled a direct evaluation of the doping/dedoping mechanisms in electropolymerized PEDOT films, revealing that small anion-doped PEDOT (PEDOT:ClO₄) differs from polyanion-doped PEDOT (PEDOT:PSS) due to the distinct involvement of dopant counterions. While EQCM-D offers valuable insights into mass transport during electrochemical processes, it presents limitations on resolving contributions from various ionic species, such as Na⁺ and ClO₄⁻, and from the solvent. As such, a more detailed understanding of mass transport will require the integration of advanced operando characterization techniques, such as XRF for substituted ions.

Discussion

We demonstrated the fabrication of highly stable organic electrochemical transistors (OECTs) via electropolymerization. OECTs based on PEDOT doped with the small anion ClO₄⁻ and the polyanion PSS⁻ exhibited high transconductance (≥ 10 mS) and ON/OFF ratios ($\sim 10^3$) in NaCl aqueous solution, comparable to state-of-the-art electrodeposited OECTs. Electropolymerization was found to significantly enhance the cycling stability of OECTs compared to devices fabricated using inkjet printing from commercially available suspensions. Notably, the incorporation of the small anion ClO₄⁻ contributed more effectively to cycling stability than the polyanion PSS⁻ and facilitated the achievement of a fully doped state in PEDOT films, which is advantageous for low-energy operation. Furthermore, a flexible, lightweight OECT was achieved by integrating electropolymerized PEDOT:ClO₄ on an ultrathin parylene substrate. The device exhibited comparable performance to the rigid counterparts, and presented unchanged electrical characteristics under mechanical bending, both parallel and perpendicular to the channel length direction, highlighting its excellent flexibility. Electrodeposition is particularly promising for the fabrication of flexible electronics, as it enables the rapid formation of

reproducible and stable devices with tunable thickness and electrical properties, while minimizing both material and solvent waste. Moreover, the technique is easily scalable, allowing for the parallel fabrication of a large number of devices.

We further investigated the ionic injection and ejection during doping/dedoping processes in electropolymerized PEDOT:ClO₄ and PEDOT:PSS films using EQCM-D. In PEDOT:PSS, the process is governed exclusively by the injection and ejection of electrolyte cations and anions, with Na⁺ playing a dominant role. For PEDOT:ClO₄, the dedoping process involves both Na⁺ ion injection from the electrolyte and the ejection of dopant ClO₄⁻ counterions, while redoping is initially governed by ejection of Na⁺ ions, followed by the re-injection of ClO₄⁻ ions.

This study demonstrates the practical application of electropolymerized PEDOT doped with small anions in flexible OECTs, highlighting its significant potential for achieving high stability across various application scenarios. Furthermore, it provides valuable insights on the complex doping/dedoping behaviors in PEDOT:ClO₄ and PEDOT:PSS films, offering a useful reference for understanding the operating mechanisms of OECTs based on different PEDOT systems. Future studies could expand the investigation to include a broader range of anions with varying ionic sizes, which would offer further insight into the size-dependent effects on device performance and doping/dedoping dynamics.

Methods

Materials

The monomer, 3,4-ethylenedioxythiophene (EDOT) (97%), was purchased from Sigma-Aldrich and stored at 4 °C. Lithium perchlorate (LiClO₄, 95.0%), poly (sodium 4-styrenesulfonate) (PSS sodium salt, Mw~1,000,000 g/mol), lithium tetrafluoroborate (LiBF₄), sodium chloride (NaCl, 99.5%), and acetonitrile (99.8%) were purchased from Sigma-Aldrich. Tetraethylammonium tetrafluoroborate (TEABF₄, 99%) was obtained from Acros Organics Chemicals. Conductive inkjet ink, poly(3,4-ethylenedioxythiophene)-poly(styrenesulfonate) (PEDOT:PSS, 0.8% in H₂O) was purchased from Sigma-Aldrich. Si/SiO₂ wafers (diameter: 100 mm) were purchased from WAFERPRO.

Rigid device fabrication

Au source and drain electrodes (W/L = 4000 $\mu\text{m}/5 \mu\text{m}$), with a layout optimized for electrodeposition experiments (Fig. 1a), were fabricated by photolithography and lift-off, as previously reported^{7,61}. The substrates were then cleaned by sequential ultra-sonication in acetone, isopropyl alcohol (IPA), and deionized (DI) water for 10 min, dried with N₂, and finally exposed to UV-Ozone cleaning (UVO-Cleaner from Jelight Company, Inc) for 20 min before electrodeposition.

Electropolymerization

Electropolymerization of PEDOT films was carried out in a three-electrode electrolyte-gated transistor bottom mount cell (redox.me, Sweden), connected to a VSP-300 Potentiostat (Bio-Logic) equipped with EC-Lab software. The source and drain electrodes, short-circuited using copper tape (3 M) and high purity silver paint (SPI supplies), served as the working electrode, a non-aqueous Ag/Ag⁺ refillable electrode (filling solution 0.01 M AgNO₃ and 0.1 M TBAP in acetonitrile, redox.me, Sweden) or an aqueous Ag/AgCl (filling solution: 3 M NaCl, ALS RE-1B, Japan) was used as the reference electrode, while a platinum coil (50HX15 0.6/250 mm, Pt 99.9%, redox. me) was used as the counter electrode. The electrolyte solution consisted of 10 mM EDOT monomer, and the desired dopant concentration, dissolved in either acetonitrile or a mixture of water and acetonitrile (details in Supplementary Table 2).

Prior to electrodeposition, the cell was purged with nitrogen for 20 min, and the nitrogen blanket was maintained during the electropolymerization to avoid undesirable oxidation reactions due to the presence of dissolved oxygen³⁶. All electrodepositions were performed in galvanostatic mode at a current density of 0.5 mA/cm²⁶². The total deposited PEDOT film area is 0.06 cm². For experiments with various dopants and concentrations, except

PSS⁻, a charge density of 60 mC/cm² was consistently achieved by depositing during 120 s. For further exploration of PEDOT:ClO₄-based devices, the deposition was conducted to reach 15 mC/cm², 30 mC/cm², and 60 mC/cm² by running for 30 s, 60 s, and 120 s, respectively^{37,63}. PEDOT:PSS OECTs were prepared by depositing at a charge density of 300 mC/cm² (600 s). Due to the limited solubility of EDOT in water and the high viscosity of the NaPSS water/acetonitrile solution, film formation proceeded slowly and non-uniformly. Under these conditions, deposition at low charge densities failed to produce a continuous film bridging the source and drain electrodes. Additionally, the smoother surface morphology of PEDOT:PSS films led to longer deposition times for the film to grow and connect the drain and source electrodes⁶³.

After electropolymerization, the films were rinsed in deionized water to remove excess solvent and salts. The copper tape was detached, and the silver paste was removed with acetone. Finally, to complete the device fabrication, Pyrex® cloning cylinders were attached to the substrate using PDMS to confine the electrolyte.

Ink-jet printing

PEDOT:PSS channels were printed using a Dimatix Materials Printer DMP-2850 (Fujifilm Dimatix), equipped with a 12-jet Samba cartridge. Prior to printing, the ink was sonicated for 1 h and then filtered using PVDF syringe filters with 0.45 μm pore size (Millex). A single layer of PEDOT:PSS was printed onto the same electrodes patterns used for electropolymerized OECTs. After printing, the samples were heated at 150 °C for 2 h on a hotplate. Finally, Pyrex® cloning cylinders were attached to the substrate to confine the electrolyte.

Flexible device fabrication

A 10 μm-thick Parylene C film was deposited onto a glass wafer to ensure rigidity during microfabrication and electrodeposition. Before photolithography, the parylene-coated wafer was sequentially rinsed with acetone, isopropanol, and deionized water, then dried under nitrogen. Gold electrodes were patterned via photolithography and lift-off using a bilayer positive tone resist. First, LOR 5 A was spin-coated at 4000 rpm for 30 s and soft-baked at 170 °C for 3 min. A top layer of OIR 674-11 was then spin-coated at 4000 rpm for 30 s and baked at 90 °C for 1.5 min. UV exposure was performed using a Karl Suss MA-6 mask aligner, followed by development in AZ-726 for 75 s. Samples were rinsed with deionized water and dried under nitrogen.

To improve metal adhesion, oxygen reactive ion etching was applied for 1 min. A 10 nm titanium adhesion layer and a 50 nm gold layer were deposited sequentially. Lift-off was achieved by immersing the wafer in Remover 1165 for 24 h, followed by thorough rinsing with deionized water.

Devices were separated using a CAMAG smartCUT cutter. Prior to electropolymerization, surface dust was removed using a gentle nitrogen flow. PEDOT:ClO₄ was electropolymerized as previously described, with a deposition charge density of 60 mC/cm² over 120 s. After electropolymerization, the parylene C film was removed from the glass, yielding flexible OECTs with electropolymerized PEDOT:ClO₄ channels. External wells to confine the electrolyte were not required as the electrolyte did not spread on the parylene substrate.

Morphology characterization

Optical Microscopy was operated on a ZEISS Axiolab microscope. A 100× objective lens was used. SEM imaging was performed on Quattro Environmental Scanning Electron Microscope (ThermoFisher Scientific). An Everhart-Thornley Detector (ETD) was used to acquire lower magnification images (5000×) at an acceleration voltage of 5 kV, while an In-Column Detector (ICD) was employed for the higher magnification images (50,000×) at an acceleration voltage of 2 kV. AFM images were obtained using the Dimension ICON-FASTSCAN AFM (Bruker) equipped with etched silicon cantilevers TESP-V2 (Bruker) in PeakForce Tapping mode in air. The images were analyzed using NanoScope Analysis software. All samples used for SEM and AFM characterizations were prepared under the same conditions as the films used for OECTs.

Device characterization

Electrical characterization of OECTs was performed with an electrical probe station (SemiProbe) connected to a NI PXIe-1062Q system (National Instruments) controlled by a customized LabView software. OECT measurements were performed using 0.1 M NaCl aqueous electrolyte and an Ag/AgCl disc (Diameter × thickness = 4 × 1 mm², Warner Instruments) as the gate electrode. Transfer curves were recorded at a constant source-drain voltage (V_D) of -0.4 V with the source-gate voltage (V_G) swept from -0.4 to 1 V or -0.6 to 0.8 V. Output curves were obtained by sweeping V_D between 0 and -0.8 V of V_D , while V_G was applied from -0.4 to 1 V or -0.6 to 0.8 V in 0.1 V steps. A sweep rate of 20 mV/s was used for both transfer and output curves. The cycling stability of the OECTs was evaluated by applying V_G square waves with an amplitude of 0.8 V (0–0.8 V) and a pulse width of 5 s for 1000 cycles.

The electrical characteristics of the flexible devices were first measured in the flat state, followed by bending tests in two directions: parallel and perpendicular to the channel length. For deformation, the flexible OECTs were mounted onto a glass rod with a diameter of 5 mm, corresponding to a bending radius of 2.5 mm in both directions, as illustrated in the insets of Fig. 3c, d. All characterization parameters were identical to those used for devices on rigid Si/SiO₂ substrates.

Spectroelectrochemistry

Spectroelectrochemistry measurements were performed with a portable potentiostat (WaveNow^{SV}, Pine Research Instrumentation, USA) in a standard three-electrode configuration. The working electrode was a PEDOT:ClO₄ film on an indium-tin-oxide (ITO) coated glass slide, the counter electrode was a platinum coil (0.6/150 mm, Pt 99.9%, redox. me), and the reference electrode was an aqueous Ag/AgCl electrode (filling solution: 3 M KCl, 6 mm diameter, 70 mm in length, redox.me). The potentiostat was coupled with a spectrometer (AvaSpec-ULS2048, Avantes) and a halogen lamp to record the absorption spectra in real time during voltage sweeps within the wavelength range from 400 to 1100 nm. To fabricate the working electrodes, ITO glass slides (SPI Supplies, 50 × 75 mm² (0.7 mm thick), 8–12 Ω) were cut into 50 × 5 mm pieces using a glass plate cutter (CAMAG smartCUT). After cleaning through sequential sonication in acetone, IPA, and DI water for 10 min, followed by a 20 min UV-Ozone treatment, PEDOT:ClO₄ films were electrodeposited on ITO glasses for 120 s using 100 mM and 5 mM dopants under the same conditions as for device fabrication. The deposition area was 1 cm². The voltage for spectroelectrochemistry (-1.0–+0.4 V) was selected to effectively capture the optical changes associated with the redox process of PEDOT. Beyond this range, no additional distinguishable changes in the optical signal were observed, indicating that extending the voltage range is unnecessary.

Electrochemical quartz crystal microbalance with dissipation (EQCM-D) measurement

EQCM-D measurements were performed using BluQCM QSD-300 (Bio-Logic) connected with an SP-200 potentiostat (Bio-Logic). QCM sensors (Bio-Logic, 5.000 MHz, 14 mm Cr/Au) were cleaned by sequentially soaking them in acetone, IPA, and DI water for 10 min, followed by 20 min UV-Ozone treatment. PEDOT films were electrodeposited on QCM sensors, which were mounted inside the AW-BEQ01Q EQCM 14 mm in-batch cell (Biologic) and used as working electrodes. A Pt coated mesh was used as the counter electrode, and a non-aqueous Ag/Ag⁺ refillable electrode (for PEDOT:ClO₄) or an aqueous Ag/AgCl electrode (for PEDOT:PSS) was used as the reference electrode. A solution of 10 mM EDOT and 100 mM of dopant was used for both PEDOT:ClO₄ and PEDOT:PSS coating. PEDOT:ClO₄-coated QCM sensors were electrodeposited at various charge densities of 15 mC/cm², 30 mC/cm², and 60 mC/cm² through running the deposition for 30 s, 60 s and 120 s, respectively. For PEDOT:PSS, the electropolymerization charge density of 15 mC/cm² was reached by 30 s of deposition.

Prior to measurements, the PEDOT-coated sensors were soaked in the 0.1 M NaCl aqueous solution for 1 h to reach equilibrium, and 20 repeated

electrochemical cycles were applied for conditioning⁵⁸. The EQCM-D responses under 5 overtones ($n = 1, 3, 5, 7$ and 9) were recorded concomitantly with cyclic voltammetry measurements between -0.8 and 0.8 V. A symmetric voltage range (-0.8 – $+0.8$ V) was selected to facilitate the analysis for reversible mass changes under balanced charge injection and repulsion conditions, allowing direct comparison for doping and dedoping behaviors. The PEDOT:ClO₄ sample electrodeposited for 30 s was measured at different scan rates of 20 mV/s, 50 mV/s, and 100 mV/s, while the other samples were measured at 50 mV/s. Data from 1st overtone is normally not considered, and the fifth overtone ($n = 9$) is not used in this work due to excessive noise.

Data availability

All the raw data that support the findings of this study are available from the corresponding author upon request.

Received: 16 May 2025; Accepted: 12 July 2025;

Published online: 26 July 2025

References

- Rivnay, J. et al. Organic electrochemical transistors. *Nat. Rev. Mater.* **3**, <https://doi.org/10.1038/natrevmats.2017.86> (2018).
- Nawaz, A., Liu, Q., Leong, W. L., Fairfull-Smith, K. E. & Sonar, P. Organic electrochemical transistors for in vivo bioelectronics. *Adv. Mater.* **33**, e2101874 (2021).
- Leleux, P. et al. Organic electrochemical transistors for clinical applications. *Adv. Healthc. Mater.* **4**, 142–147 (2015).
- Marks, A., Griggs, S., Gasparini, N. & Moser, M. Organic electrochemical transistors: an emerging technology for biosensing. *Adv. Mater. Interfaces* **9**, <https://doi.org/10.1002/admi.202102039> (2022).
- Harikesh, P. C. et al. Organic electrochemical neurons and synapses with ion mediated spiking. *Nat. Commun.* **13**, 901 (2022).
- van de Burgt, Y. et al. A non-volatile organic electrochemical device as a low-voltage artificial synapse for neuromorphic computing. *Nat. Mater.* **16**, 414–418 (2017).
- Azimi, M., Subramanian, A., Fan, J., Soavi, F. & Cicoira, F. Electrical and mechanical stability of flexible, organic electrolyte-gated transistors based on iongel and hydrogels. *J. Mater. Chem. C* **11**, 4623–4633 (2023).
- Paulsen, B. D., Tybrandt, K., Stavrinidou, E. & Rivnay, J. Organic mixed ionic-electronic conductors. *Nat. Mater.* **19**, 13–26 (2020).
- Torricelli, F. et al. Electrolyte-gated transistors for enhanced performance bioelectronics. *Nat. Rev. Methods Primers* **1**, <https://doi.org/10.1038/s43586-021-00065-8> (2021).
- Khodagholy, D. et al. High transconductance organic electrochemical transistors. *Nat. Commun.* **4**, 2133 (2013).
- Rivnay, J. et al. Organic electrochemical transistors with maximum transconductance at zero gate bias. *Adv. Mater.* **25**, 7010–7014 (2013).
- Zhang, S. et al. Solvent-induced changes in PEDOT:PSS films for organic electrochemical transistors. *APL Mater.* **3**, <https://doi.org/10.1063/1.4905154> (2015).
- Kim, S. M. et al. Influence of PEDOT:PSS crystallinity and composition on electrochemical transistor performance and long-term stability. *Nat. Commun.* **9**, 3858 (2018).
- Rivnay, J. et al. Structural control of mixed ionic and electronic transport in conducting polymers. *Nat. Commun.* **7**, 11287 (2016).
- Romele, P., Ghittorelli, M., Kovacs-Vajna, Z. M. & Torricelli, F. Ion buffering and interface charge enable high performance electronics with organic electrochemical transistors. *Nat. Commun.* **10**, 3044 (2019).
- Wang, S. et al. An organic electrochemical transistor for multi-modal sensing, memory and processing. *Nat. Electron.* **6**, 281–291 (2023).
- Zabhipour, M. et al. High yield manufacturing of fully screen-printed organic electrochemical transistors. *npj Flex. Electron.* **4**, <https://doi.org/10.1038/s41528-020-0078-9> (2020).
- Kim, C. H. et al. All-printed and stretchable organic electrochemical transistors using a hydrogel electrolyte. *Nanoscale* **15**, 3263–3272 (2023).
- Fan, J., Montemagno, C. & Gupta, M. 3D printed high transconductance organic electrochemical transistors on flexible substrates. *Org. Electron.* **73**, 122–129 (2019).
- Basiricò, L. et al. Electrical characteristics of ink-jet printed, all-polymer electrochemical transistors. *Org. Electron.* **13**, 244–248 (2012).
- Fan, J., Forero Pico, A. A. & Gupta, M. A functionalization study of aerosol jet printed organic electrochemical transistors (OECTs) for glucose detection. *Mater. Adv.* **2**, 7445–7455 (2021).
- White, H. S., Kittlesen, G. P. & Wrighton, M. S. Chemical derivatization of an array of three gold microelectrodes with polypyrrole: fabrication of a molecule-based transistor. *J. Am. Chem. Soc.* **106**, 5375–5377 (1984).
- Paul, E. W., Ricco, A. J. & Wrighton, M. S. Resistance of polyaniline films as a function of electrochemical potential and the fabrication of polyaniline-based microelectronic devices. *J. Phys. Chem.* **89**, 1441–1447 (1985).
- Thackeray, J. W., White, H. S. & Wrighton, M. S. Poly (3-methylthiophene)-coated electrodes: optical and electrical properties as a function of redox potential and amplification of electrical and chemical signals using poly (3-methylthiophene)-based microelectrochemical transistors. *J. Phys. Chem.* **89**, 5133–5140 (1985).
- Thackeray, J. W. & Wrighton, M. S. Chemically responsive microelectrochemical devices based on platinumized poly (3-methylthiophene): variation in conductivity with variation in hydrogen, oxygen, or pH in aqueous solution. *J. Phys. Chem.* **90**, 6674–6679 (1986).
- Gerasimov, J. Y. et al. A biomimetic evolvable organic electrochemical transistor. *Adv. Electron. Mater.* **7**, <https://doi.org/10.1002/aelm.202001126> (2021).
- Gerasimov, J. Y. et al. An evolvable organic electrochemical transistor for neuromorphic applications. *Adv. Sci.* **6**, 1801339 (2019).
- Janzakova, K. et al. Dendritic organic electrochemical transistors grown by electropolymerization for 3d neuromorphic engineering. *Adv. Sci.* **8**, e2102973 (2021).
- Cucchi, M. et al. Directed growth of dendritic polymer networks for organic electrochemical transistors and artificial synapses. *Adv. Electron. Mater.* **7** <https://doi.org/10.1002/aelm.202100586> (2021).
- Wustoni, S. et al. In situ electrochemical synthesis of a conducting polymer composite for multimetabolite sensing. *Adv. Mater. Technol.* **5**, <https://doi.org/10.1002/admt.201900943> (2019).
- Fenoy, G. E. et al. “Clickable” organic electrochemical transistors. *J. Am. Chem. Soc.* **2**, 2778–2790 (2022).
- Fenoy, G. E. et al. Interface engineering of “clickable” organic electrochemical transistors toward biosensing devices. *ACS Appl. Mater. Interfaces* **15**, 10885–10896 (2023).
- Fenoy, G. E. et al. A poly(3,4-ethylenedioxythiophene) derivative incorporating ethynyl moieties for click chemistry-based bioelectronics. *Chem. Mater.* **36**, 7207–7221 (2024).
- Brodsky, J. et al. Downsizing the channel length of vertical organic electrochemical transistors. *ACS Appl. Mater. Interfaces* **15**, 27002–27009 (2023).
- Hagler, J. E. et al. Electrodeposited PEDOT:BF₄ coatings improve impedance of chronic neural stimulating probes in vivo. *Adv. Mater. Interfaces* **9**, <https://doi.org/10.1002/admi.202201066> (2022).
- Bodart, C. et al. Electropolymerized poly(3,4-ethylenedioxythiophene) (PEDOT) coatings for implantable deep-brain-stimulating microelectrodes. *ACS Appl. Mater. Interfaces* **11**, 17226–17233 (2019).

37. Lee, J. et al. Electrochemical fabrication and characterization of organic electrochemical transistors using poly(3,4-ethylenedioxythiophene) with various counterions. *ACS Appl. Mater. Interfaces* **14**, 42289–42297 (2022).
38. Flagg, L. Q. et al. Polymer crystallinity controls water uptake in glycol side-chain polymer organic electrochemical transistors. *J. Am. Chem. Soc.* **141**, 4345–4354 (2019).
39. Wu, R., Paulsen, B. D., Ma, Q. & Rivnay, J. Mass and charge transport kinetics in an organic mixed ionic–electronic conductor. *Chem. Mater.* **34**, 9699–9710 (2022).
40. Savva, A., Wustoni, S. & Inal, S. Ionic-to-electronic coupling efficiency in PEDOT:PSS films operated in aqueous electrolytes. *J. Mater. Chem. C.* **6**, 12023–12030 (2018).
41. Zhang, L. & Andrew, T. L. Deposition dependent ion transport in doped conjugated polymer films: insights for creating high-performance electrochemical devices. *Adv. Mater. Interfaces* **4**, <https://doi.org/10.1002/admi.201700873> (2017).
42. Wu, R., Paulsen, B. D., Ma, Q., McCulloch, I. & Rivnay, J. Quantitative composition and mesoscale ion distribution in p-type organic mixed ionic–electronic conductors. *ACS Appl. Mater. Interfaces* **15**, 30553–30566 (2023).
43. Murugappan, K. & Castell, M. R. Bridging electrode gaps with conducting polymers around the electrical percolation threshold. *Electrochem. Commun.* **87**, 40–43 (2018).
44. Janzakova, K. et al. Analog programming of conducting-polymer dendritic interconnections and control of their morphology. *Nat. Commun.* **12**, 6898 (2021).
45. Koizumi, Y. et al. Electropolymerization on wireless electrodes towards conducting polymer microfibre networks. *Nat. Commun.* **7**, 10404 (2016).
46. Ghazal, M. et al. Bio-inspired adaptive sensing through electropolymerization of organic electrochemical transistors. *Adv. Electron. Mater.* **8**, <https://doi.org/10.1002/aelm.202100891> (2021).
47. Zhang, S. et al. Intrinsically antifouling, soft and conformal bioelectronic from scalable fabrication of thin-film OECT arrays by zwitterionic polymers. *Chem. Eng. J.* **483**, <https://doi.org/10.1016/j.cej.2024.148980> (2024).
48. Rajapakse, R. M. G. et al. Implementing the donor–acceptor approach in electronically conducting copolymers via electropolymerization. *RSC Adv.* **12**, 12089–12115 (2022).
49. Musumeci, C., Hutchison, J. A. & Samori, P. Controlling the morphology of conductive PEDOT by in situ electropolymerization: from thin films to nanowires with variable electrical properties. *Nanoscale* **5**, 7756–7761 (2013).
50. Poverenov, E., Li, M., Bitler, A. & Bendikov, M. Major effect of electropolymerization solvent on morphology and electrochromic properties of PEDOT Films. *Chem. Mater.* **22**, 4019–4025 (2010).
51. Xie, M. et al. Cycling stability of organic electrochemical transistors. *Org. Electron.* **117**, <https://doi.org/10.1016/j.orgel.2023.106777> (2023).
52. Szumska, A. A. et al. Reversible electrochemical charging of n-type conjugated polymer electrodes in aqueous electrolytes. *J. Am. Chem. Soc.* **143**, 14795–14805 (2021).
53. Modarresi, M., Mehandzhyski, A., Fahlman, M., Tybrandt, K. & Zozoulenko, I. Microscopic understanding of the granular structure and the swelling of PEDOT:PSS. *Macromolecules* **53**, 6267–6278 (2020).
54. Li, Y. et al. Tailoring the self-healing properties of conducting polymer films. *Macromol. Biosci.* **20**, e2000146 (2020).
55. Bargigia, I., Savagian, L. R., Osterholm, A. M., Reynolds, J. R. & Silva, C. Charge-transfer intermediates in the electrochemical doping mechanism of conjugated polymers. *J. Am. Chem. Soc.* **143**, 294–308 (2021).
56. Massonnet, N. et al. Improvement of the Seebeck coefficient of PEDOT:PSS by chemical reduction combined with a novel method for its transfer using free-standing thin films. *J. Mater. Chem. C.* **2**, 1278–1283 (2014).
57. Levi, M. D. et al. In situ porous structure characterization of electrodes for energy storage and conversion by EQCM-D: a review. *Electrochim. Acta* **232**, 271–284 (2017).
58. Easley, A. D. et al. A practical guide to quartz crystal microbalance with dissipation monitoring of thin polymer films. *J. Polym. Sci.* **60**, 1090–1107 (2021).
59. Reviakine, I., Johannsmann, D. & Richter, R. P. Hearing what you cannot see and visualizing what you hear: interpreting quartz crystal microbalance data from solvated interfaces. *Anal. Chem.* **83**, 8838–8848 (2011).
60. Kumar, P. et al. Effect of channel thickness, electrolyte ions, and dissolved oxygen on the performance of organic electrochemical transistors. *Appl. Phys. Lett.* **107**, <https://doi.org/10.1063/1.4927595> (2015).
61. Azimi, M., Subramanian, A., Roslan, N. A. & Cicoira, F. Flexible organic ion-gated transistors with low operating voltage and light-sensing application. *J. Phys.* **4**, <https://doi.org/10.1088/2515-7639/abd018> (2021).
62. King, Z. A., Shaw, C. M., Spanninga, S. A. & Martin, D. C. Structural, chemical and electrochemical characterization of poly(3,4-ethylenedioxythiophene) (PEDOT) prepared with various counter-ions and heat treatments. *Polymer* **52**, 1302–1308 (2011).
63. Boz, E. B., Fritz, M. & Forner-Cuenca, A. Electropolymerized poly(3,4-ethylenedioxythiophene) coatings on porous carbon electrodes for electrochemical separation of metals. *Adv. Mater. Interfaces* **10**, <https://doi.org/10.1002/admi.202202497> (2023).

Acknowledgements

This research was supported by the Natural Science and Engineering Council Canada (NSERC) through Discovery Grants awarded to F.C. and J.M. and National Defense Canada (IDEaS project CFPMN1-008, awarded to F.C.). The equipment and infrastructure used in this study were acquired and maintained by the Canada Foundation for Innovation. M.W. acknowledges Fonds de recherche du Québec (FRQNT) for a Doctoral Research Scholarship. J.F. acknowledges support from the NSERC Postdoctoral Fellowship.

Author contributions

F.C. and J.M. supervised the research, contributed to discussions and manuscript editing. M.W. conducted the experiments, analyzed the results and drafted the manuscript. J.F. did data analysis and edited the manuscript. M.B.-C. provided the protocol for electropolymerization. C.K. reviewed the manuscript. C.-L.C. and A.F.C.S. assisted in conducting experiments. V.V. and I.B. performed the spectroelectrochemistry tests, contributed to results discussions and manuscript editing. All the authors read and revised the manuscript.

Competing interests

The authors declare no competing interests.

Additional information

Supplementary information The online version contains supplementary material available at <https://doi.org/10.1038/s41528-025-00457-w>.

Correspondence and requests for materials should be addressed to Fabio Cicoira.

Reprints and permissions information is available at <http://www.nature.com/reprints>

Publisher's note Springer Nature remains neutral with regard to jurisdictional claims in published maps and institutional affiliations.

Open Access This article is licensed under a Creative Commons Attribution-NonCommercial-NoDerivatives 4.0 International License, which permits any non-commercial use, sharing, distribution and reproduction in any medium or format, as long as you give appropriate credit to the original author(s) and the source, provide a link to the Creative Commons licence, and indicate if you modified the licensed material. You do not have permission under this licence to share adapted material derived from this article or parts of it. The images or other third party material in this article are included in the article's Creative Commons licence, unless indicated otherwise in a credit line to the material. If material is not included in the article's Creative Commons licence and your intended use is not permitted by statutory regulation or exceeds the permitted use, you will need to obtain permission directly from the copyright holder. To view a copy of this licence, visit <http://creativecommons.org/licenses/by-nc-nd/4.0/>.

© The Author(s) 2025